RSC Sustainability

PAPER

View Article Online
View Journal | View Issue

Check for updates

Cite this: *RSC Sustainability*, 2023, **1**, 622

Dual heterojunction-based Au@TiO$_2$ photoelectrode exhibiting efficient charge separation for enhanced removal of organic dye under visible light†

Pan Zhang,[a] Yuzhou Jin,[a] Mingfang Li,[a] Xuejiang Wang[b] and Ya-nan Zhang *[a]

Received 5th January 2023
Accepted 15th March 2023

DOI: 10.1039/d3su00006k

rsc.li/rscsus

An inventive strategy that involves photo-deposition of Au nanoparticles (NPs) on the flower-like TiO$_2$ nanomicrospheres with co-exposed {001} and {101} facets was reported to construct an advanced visible-light responsive Au@A-FH TiO$_2$/Ti photoelectrode. The plasmonic Au NPs lead to the effective utilization of visible light. The plasmonic Au NPs generate hot e$^-$ under visible light and then ransferred to TiO$_2$ through the Au/TiO$_2$ Schottky junction, which finally reach the Ti substrate along the {001}/{101} facet heterojunction (FH). The *in situ* Kelvin probe force microscopy (KPFM) technology measured the high-resolution contact potential difference (CPD) images between the single Au NP region and the surrounding TiO$_2$ under the visible light, indirectly visualizing the different electron transfer directions between single Au NP and TiO$_2$. Quantitative calculations revealed improved light absorption, charge separation, and surface charge injection efficiency due to the presence of dual heterojunctions (Au/TiO$_2$ Schottky junction and {001}/{101} FH), which together account for high PEC efficiency. The obtained Au@A-FH TiO$_2$/Ti shows high PEC performance under visible light, achieving almost 100% removal of methyl orange (MO) within 2 h. This study provides a set of reliable experimental evidence to verify the electron transfer direction and photoelectrocatalytic mechanism and also offers a new avenue for the design of an efficient TiO$_2$-based visible-light responsive photoelectrode.

Sustainability spotlight

With the intensive development of dyeing, printing, and leather industries, organic dyestuff-based industrial wastewater has caused serious damage to water resources; it is necessary to develop innovative methods to efficiently remove organic dyes in wastewater. The continuing progress of this work is that it proposes an advanced PEC oxidation strategy for enhanced oxidation and complete mineralization of methyl orange under visible light, which depends on the novel Au@TiO$_2$ photoelectrode with dual heterojunctions (Au/TiO$_2$ Schottky junction as well as facet heterojunction). This work is in line with Goal 6 "Clean Water" and 9 "Industrial Innovation".

1. Introduction

Against the backdrop of the global ecological water crisis, achieving efficient wastewater treatment and restoration has become an urgent task. As a novel effluent treatment technology, advanced oxidation processes (AOPs) can achieve deep mineralization of pollutants by producing reactive oxygen species (ROS).[1,2] Common AOP technologies include ultrasonic oxidation, O$_3$ oxidation, electrocatalysis or photocatalysis; however, they exhibit high energy consumption, easy decomposition (O$_3$ decomposes to O$_2$ in air and water) and poor photoelectric convertibility.[3–6] Among AOPs, PEC technology can produce ROS *in situ* by converting sunlight and applying a bias voltage to massively generate and rapidly separate charges without adding an external catalyst.[7,8] The advantages of PEC systems lies in the maximum photocurrent (J_{ph}) can be generated under the minimal bias. This can be achieved by applying photoelectrode materials with the suitable E_g to obtain the highest η_{abs} (light absorption efficiency), the best η_{sep} (charge separation efficiency) the maximum η_{inj} (the efficiency of photogenerated holes injected to the surface reaction).[9–11] Therefore, seeking a suitable photoelectrode material is particularly critical.

Anatase TiO$_2$ has gained increasing interest because of its low cost, high chemical stability and non-poisonous nature.[12,13] Owing to the wide band gap of anatase TiO$_2$ (3.2 eV), it is limited

---

[a] *School of Chemical Science and Engineering, Shanghai Key Lab of Chemical Assessment and Sustainability, Key Laboratory of Yangtze River Water Environment, Tongji University, Shanghai 200092, People's Republic of China. E-mail: yananzhang@tongji.edu.cn*

[b] *College of Environmental Science and Engineering, Shanghai Institute of Pollution Control and Ecological Security, Tongji University, Shanghai 200092, PR China*

† Electronic supplementary information (ESI) available. See DOI: https://doi.org/10.1039/d3su00006k

to harvesting UV light, which accounts for a tiny fraction of sunlight. Several methods have been proposed to extend the light absorptivity performance of TiO_2, including complication of noble metal nanoparticles (NPs), fabrication of defect states, and sensitization of low-bandgap semiconductors.[14–16] Recently, complication of noble metal NPs (*e.g.*, Au, Ag and Pt) has been proposed to extend the light absorption properties of TiO_2 owing to their localized surface plasmon resonance (LSPR) effect under certain wavelengths of light excitation.[17,18] In particular, Au nanoparticles (NPs) have attracted considerable attention owing to their strong visible light-harvesting ability and high stability. It is claimed that the plasma metal–semiconductor interaction between Au and TiO_2 yields the Schottky junction, which facilitates the hot e^- transmission from Au NPs to TiO_2.[19] Further, note that TiO_2 still suffers from low quantum inefficiency, the electrons arriving at TiO_2 tend to recombinant with each other, leaving a pressing challenge of low η_{sep}. Constructiing heterogeneous structured photoelectrodes is a method for achieving effective η_{sep}.[20–22] At present, it has been recognized that the crystal facet engineering of TiO_2 can also significantly enhance interfacial activity without the introduction of exotic materials, extraordinarily when exposing two facets with multiple band positions matching from one another.[23,24] The co-exposed facets form the facet heterojunction (FH), offering intrinsic motivation for the ordered separation of charges. Our recent work found that the anatase TiO_2 {001} and {101} facets constitute a typical FH, inducing more photogenerated electron switching from the {001} facet to the {101} facet, thus improving the η_{sep}.[25,26] Therefore, it is promising to load Au NPs onto FH TiO_2, the Au NPs composition enables TiO_2 to absorb visible light, and the dualle heterojunctions system between Au–TiO_2 Schottky junction and {001}–{101} FH achieves rapid separation of photogenerated charges, and the active crystal surface of FH TiO_2 promotes the continuous injection of holes, ultimately constructing a high PEC performance photoelectrode.

Herein, we propose to obtain Au@A-FH TiO_2/Ti by the photodeposition of Au NPs on the surface of anatase TiO_2 nano–microspheres with {001}/{101} FH. First, the LSPR effect of Au NPs enables the photoelectrode to capture visible light, which significantly extends the visible-light harvesting ability of the photoelectrode. Second, the Au-excited high-energy electrons cross the Au–TiO_2 Schottky junction to TiO_2, then complete secondary separation along {001}–{101} FH and reach the counter electrode. Finally, the Ti mesh facilitates the fast mass transportation of the solution and effectively increases the area of contact between the contaminant and photoelectrode. The PEC oxidation performance of the photoelectrode was evaluated by eliminating the typical organic dye MO and other non-dye pollutants.

2. Experimental

2.1 Materials

Bisphenol A (≥99.5%), hydrofluoric acid (HF, ≥38.0%), methyl alcohol (CH_3OH, >99.9%), nitric acid (HNO_3, 65.0–68.0%) and isopropyl alcohol (IPA, >99.0%) were all provided by Sinopharm (Shanghai, China). Absolute ethyl alcohol (CH_3CH_2OH, >99.9%), anhydrous sodium sulfate (Na_2SO_4, >99.0%) and anhydrous sodium sulphite (Na_2SO_3, >99.0%) were obtained from Titan Technologies Inc. (Shanghai, China). Chloroauric acid hydrate ($HAuCl_4 \cdot xH_2O$, Au: 50%) was bought from Adamas Reagent Co., Ltd. (Shanghai, China). Titanium foil substrate (80 mesh, 0.1 mm in diameter, ≥99.99%) was obtained from Anping Kangwei Wire Mesh Products Co., Ltd. The PTFE hydrothermal kettle was purchased from ShanghaiYanzheng Experimental Instrument Co., Ltd. All reagents were used without further purification.

2.2 Synthesis of Au@A-FH TiO_2/Ti and Au@A-TiO_2/Ti

The titanium mesh substrate needs to be pretreated before participating in the hydrothermal reaction: 3.5 × 5 cm Ti mesh was put into the mixed solution ($V_{H_2O} : V_{HNO_3} : V_{HF} = 20 : 5 : 1$) for nearly 30 s and then removed. The obtained Ti mesh was immediately placed into DI water and anhydrous ethanol to ultrasonically clean for 5 minutes each and finally reserved it in ethanol solution for further use. 30 mL DI water and 27 μL HF were added into a 100 mL PTFE hydrothermal kettle sequentially, and the solution was stirred well and then put into the pre-processed Ti mesh. The hydrothermal reaction was carried out at 180 °C for 3 h. Similarly, the pre-treated Ti network was placed in 100 mL H_2O_2 solution and heated at 100 °C for 1 h. The precursors were cleaned with deionized water and reserved as A-FH TiO_2/Ti and A-TiO_2/Ti.

The Au NPs were loaded using the photo-deposition method. The obtained A-FH TiO_2/Ti photoelectrode was deposited into a mixture of 100 mL H_2O, 5 mL CH_3OH and 70 μL (or 35 μL and 140 μL) $HAuCl_4 \cdot 4H_2O$ (1 wt%), which were irradiated under a xenon lamp (300 W) and stirred for 1 h. The samples were washed with deionized water and dried at 70 °C for 3 h. The photoelectrodes were then calcined at 450 °C for 3 h in the air (the heating rate was 3 °C min^{-1}). The final photoelectrodes are named as 1%Au@A-FH TiO_2/Ti (35 μL), 2%Au@A-FH TiO_2/Ti (70 μL) and 4%Au@A-FH TiO_2/Ti (140 μL). Subsequently, the optimal Au loading was combined with the A-TiO_2/Ti to obtain the Au@A-TiO_2/Ti contrast photoelectrode.

2.3 Characterization

The topography structure and elemental content of the prepared photoelectrodes were characterized by field emission scanning electron microscopy (SEM, Hitachi-S4800), transmission electron microscopy (TEM, JEM-2100, JEOL) and energy spectrometry (EDS). The elemental valence states on the surface of the photoelectrodes were characterized by X-ray photoelectron spectroscopy (XPS, $<10^{-8}$ torrent, Al target, 150 W, AXIS Ultra DLD, Shimazu Kratos). XRD diffraction spectroscopy (D8-A25‖ ‖, Bruker) was used to characterize the crystalline shape of the photoelectrodes. The UV-vis absorption range of the photoelectrodes was tested using UV-vis diffuse reflectance spectroscopy (Agilent Carry 5000).

2.4 PEC performance test

Photoelectrochemical (PEC) characterization was performed using a standard three-electrode system through the CHI660E electrochemical workstation. The obtained photoelectrodes, platinum sheet and saturated calomel electrode (SCE) were used as the working electrodes, counter electrode and reference electrode, respectively. The electrolyte was 0.1 mol L^{-1} of Na_2SO_4 solution. NBeT Solar-500 Xe lamp plus a visible light filter (>420 nm) was used as the light source.

2.5 Photoelectrocatalytic experiments

The PEC degradation of MO, phenol and BPA was accomplished by HDY-I potentiostat with the +0.4 V *vs.* SCE bias voltage and the 50 mL degradation device square double-layered quartz reactor with the external condensate flow, ensuring that the temperature of the system was maintained at room temperature throughout the degradation process. The 45 mL degradation solution contained 5 mg L^{-1} MO and 0.1 mol L^{-1} Na_2SO_4. The initial concentration of phenol and BPA was 1 mg L^{-1}. The light source was a 300 W xenon lamp (PLS-SXE 300) plus a visible light filter (>420 nm) whose output light intensity was 520 mW cm^{-2}. The concentration variations of MO, phenol and BPA during the reaction were determined by applying a UV spectrophotometer (UV-1800), GC (Shimadzu 2014) and HPLC (Agilent 1260). Total organic carbon (TOC) in the post-reaction solution was determined using a total organic carbon analyzer (multi N/C 3100, Analytik Jena, Germany). The scavenging experiment was conducted under the same conditions of PEC degradation, except for adding isopropyl alcohol (IPA) and plenty of nitrogen (N_2) as the scavengers of $^{\bullet}OH$ and $^{\bullet}O_2^{-}$, respectively.

2.6 KPFM measurement

The A-FH TiO_2/Ti powder distributed in the hydrothermal reaction solution was collected by centrifugal drying. 20 mg A-FH TiO_2/Ti powder and 40 mg iodine were dissolved in 100 mL acetone. The FTO substrate and Pt sheet were used separately as the cathode and counter electrode. The uniformly distributed A-FH TiO_2/Ti-FTO photoelectrode was energized at an applied potential of +15 V for 15 min. Through the same photoreductive deposition process, the Au@A-FH TiO_2/Ti-FTO was obtained and used for KPFM characterization.

The spatial morphology and contact potential difference (CPD), *i.e.*, the surface potential, of the Au@A-FH TiO_2/Ti-FTO in atmospheric conditions were measured sequentially using KPFM in tap mode. Pt/Ir coated silicon Tips (SCM-PIT-V2) were used as Kelvin tips. UV and visible light incidents perpendicular to the substrate were used to measure the CPD under illumination. The CPD is defined as follows:

$$V_{CPD} = (W_s - W_t)/e,$$

where W_s and W_t are the work functions of the sample and tip surface, respectively.

3. Results and discussion

3.1 Topography characterization and compositional analyses

The TiO_2 flower-like microspheres (A-FH TiO_2/Ti) were grown *in situ* on the Ti mesh substrate by applying the hydrothermal method, each with a size of 600–800 nm and consisting of truncated tetra-pyramidal TiO_2 nanocrystals (Fig. 1a1 and a2). The relevant morphologies of x%Au@A-FH TiO_2/Ti ($x = 1, 2, 4$) in Fig. 1b1–d2 shows the average size of Au NPs increases gradually with an increased concentration of Au precursor solution ($HAuCl_4 \cdot xH_2O$) from 1% to 4%. Among them, 2%Au@A-FH TiO_2/Ti shows the most uniform distribution in which the Au NPs are evenly coated on the TiO_2 microspheres surface (Fig. 1b and S1†), while for 4%Au@A-FH TiO_2/Ti (Fig. 1d), the Au NPs tend to agglomerate and obscure TiO_2 microspheres. The HRTEM images taken at the 2%Au@A-FH TiO_2/Ti (Fig. 1e and f) further confirm the effective loading of Au NPs. The Au particle size distribution, as shown in Fig. S2,† displays that the average size of Au NPs is around 15.7 nm. The HRTEM, as illustrated in Fig. 1g, exhibits that the interplanar crystal spacing is 0.351 nm, corresponding to the {101} facet of anatase TiO_2, which can be inferred as the side facet of typical truncated pyramidal.[27] The angle between the side facet and the top cross-facet is 122.5°, combined with the model schematic (Fig. S3, ESI†) to determine the top cross-facet is {001} facet.[28,29] The exposure percentage of {001} facet is calculated to be approximately 70%, which results in more Au NPs being deposited to the {001} facet.[30,31] The well-identified lattice spacings of 0.235 nm on the nanoparticles (Fig. 1h) correspond to the {111} facet of cubic Au.[32]

The X-ray diffraction (XRD) pattern (Fig. S4a, ESI†) shows characteristic peaks at 62.7°, 48°, 37.8° and 25.3°, attributing to the (204), (200), (004) and (101) planes of anatase TiO_2 (JCPDS no. 21-1272), respectively, indicating that A-FH TiO_2 is highly crystalline with anatase structure.[33] Compared with the pristine A-FH TiO_2, the characteristic crystal phases remain the same after Au loading, except that the intensity of individual peaks is appropriately weakened. The Raman spectra show that the vibrational peaks of all samples belong to the anatase phase of TiO_2 (Fig. S4b†).[34] Few vibrational peaks belong to Au presumably due to the low content and good dispersion of Au NPs.

X-Ray photoelectron spectroscopy (XPS) was employed to illustrate the elemental composition and chemical states of A-FH TiO_2/Ti before and after Au NPs deposition (Fig. 2a); the statistics are listed in Table S2 (ESI†). The characteristic peaks of Ti 2p and O 1s show a positive shift of 0.2 eV and 0.3 eV after Au deposition, respectively (Fig. 2b and c). This suggests the loss of electrons from the Ti and O atoms.[35] In addition, the deposition of Au leads to a decrease in the raw area ratio of peak Ti–O–H to peak Ti–O–Ti, which correlates with the tiny quantities of oxygen vacancies (V_O), indicating that Au NPs are preferentially deposited at the surface V_O sites.[36] The Au 4f spectra of Au@A-FH TiO_2/Ti shows two significant peaks at 83.0 eV and 86.8 eV, attributing to Au^0 $4f_{7/2}$ and Au^0 $4f_{5/2}$, which demonstrates the free metallic state of Au NPs. Notably, the peak of Au^0 $4f_{7/2}$ (83.0 eV) is lower than that of the bulk Au (∼83.8 eV),[37] such a change can be explained by the strong Au/TiO_2 interaction, which induces the electron transfer from TiO_2 to Au in the dark.

3.2 Photochemical property of photoelectrodes

To illustrate the photoelectric conversion capability, the linear sweep voltammograms (LSV) and I–t curves of prepared photoelectrodes under visible-light excitation are shown in Fig. 3a

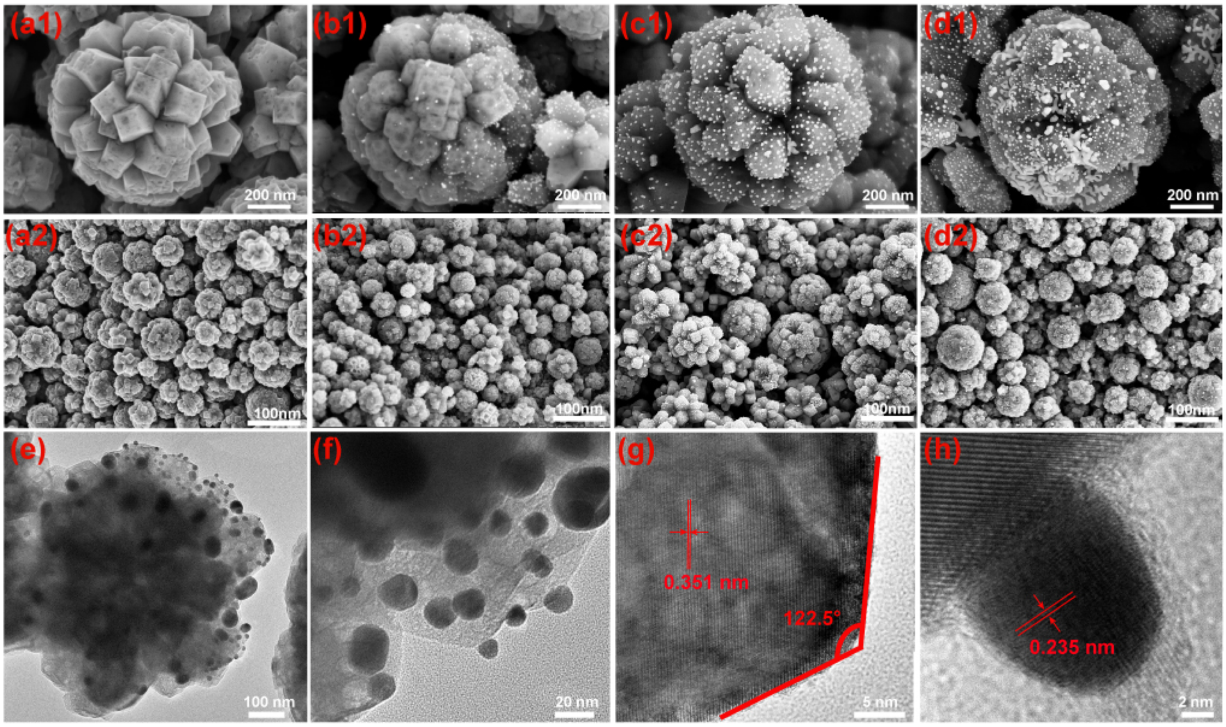

Fig. 1 (a1–d2) SEM images of A-FH TiO_2/Ti, 1%Au@A-FH TiO_2/Ti, 2%Au@A-FH TiO_2/Ti and 4%Au@A-FH TiO_2/Ti. (e–h) HRTEM images of 2% Au@A-FH TiO_2/Ti.

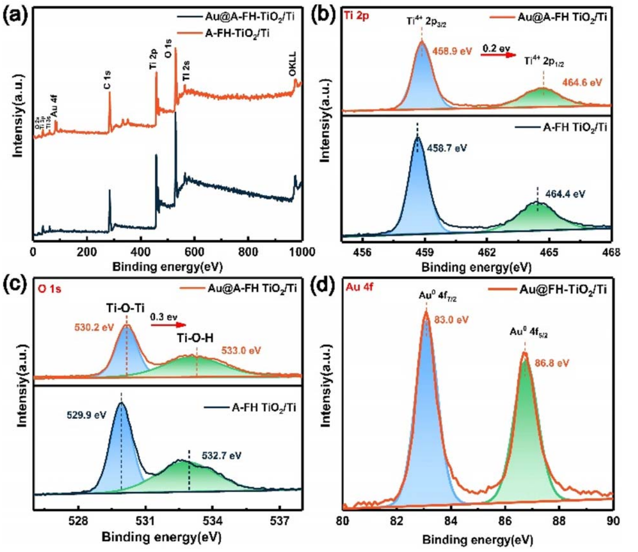

Fig. 2 The XPS spectra (a), Ti 2p (b), O 1s (c) and Au 4f (d) spectra of A-FH TiO_2/Ti and Au@A-FH TiO_2/Ti.

and b, and the relevant data are displayed in Table S1 (ESI†). In all cases, the modified Au@A-FH TiO_2/Ti photoelectrode exhibits higher photocurrent density than the unmodified counterparts. Moreover, the photocurrent density of 2%Au@A-FH TiO_2/Ti reached the maximum value (1.15×10^{-5} A cm^{-2}) after three on/off light cycles, which was 1.6, 1.5 and 1.3 times that of A-FH TiO_2/Ti, 1%Au@A-FH TiO_2/Ti and 4%Au@A-FH TiO_2/Ti, respectively. Fig. 3c shows the Mott–Schottky plots produced by the capacitance values. The straight lines of all the photoelectrodes represent positive slopes, indicating typical n-type semiconductor characteristics. Compared to the others, 2%Au@A-FH TiO_2/Ti shows the highest carrier concentration (2.67×10^{20} cm^{-3}). As displayed in the typical Nyquist plots (Fig. 3d), the charge transfer impedance of 2%Au@A-FH TiO_2/Ti is 5 kΩ, which is significantly smaller than those of 4%Au@A-

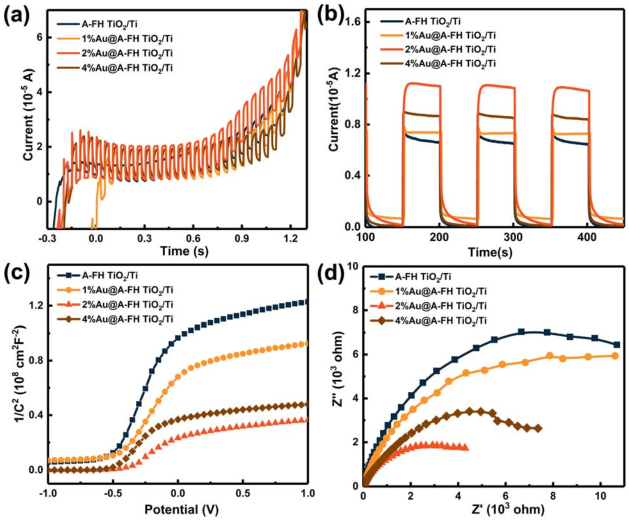

Fig. 3 LSV (a) and *i*–*t* curves (b) of A-FH TiO_2/Ti, 1%Au@A-FH TiO_2/Ti, 2%Au@A-FH TiO_2/Ti and 4%Au@A-FH TiO_2/Ti. Mott–Schottky plots (c) and EIS responses (d) of the prepared photoelectrodes under visible-light excitation.

FH TiO_2/Ti (7.5 kΩ), 1%Au@A-FH TiO_2/Ti (12 kΩ) and A-FH TiO_2/Ti (14 kΩ), suggesting faster charge transfer dynamics. The above results confirm that 2%Au@A-FH TiO_2/Ti represents the highest photoelectric response and charge separation efficiency, which is used as the optimal photoelectrode for further study.

3.3 The η_{abs}, η_{sep} and η_{inj} of photoelectrodes

To illustrate the role of Au NPs and facet heterojunction (FH) for PEC performance in detail, A-FH-TiO_2 and Au@A-TiO_2/Ti (non-specific facet anatase TiO_2 loaded with Au NPs in Fig. S5, ESI†) are served as contrast photoelectrodes. The light absorption properties were first investigated by UV-vis diffuse reflectance measurement. As shown in Fig. 4a, in contrast with A-FH TiO_2/Ti, the Au NP decoration leads to an extra absorption peak at 550 nm for both Au@A-TiO_2/Ti and Au@A-FH TiO_2/Ti. This clearly originates from the LSPR effect of Au NPs. Moreover, the absorption intensity of Au@A-FH TiO_2/Ti is significantly enhanced once the facet heterojunction between {001} and {101} facets of TiO_2 ({001}/{101} FH) is introduced as opposed to Au@A-TiO_2/Ti. As depicted in Fig. 4b, the η_{abs} of the three samples were obtained based on the LSV curves using the following equation:

$$\eta_{abs} = 1 - 10^{-J_{light}} \tag{1}$$

where J_{light} is the photocurrent of LSV in 0.1 M Na_2SO_4 aqueous solution under AM1.5G illumination (Fig. S6a, ESI†). The results are shown in Table S3 (ESI†).[38] The η_{abs} for Au@A-FH TiO_2/Ti (54.5%) is significantly higher than those of A-FH TiO_2/Ti (45.2%) and Au@A-FH TiO_2/Ti (32.6%) at the reaction potential of +0.4 V. Fig. 4c further depicts the electron lifetimes (τ) by normalizing the open-circuit potential (V_{oc}) curves.[39] Au@A-FH TiO_2/Ti exhibits a prolonged lifetime than that of A-FH TiO_2/Ti and Au@A-TiO_2/Ti under the same V_{oc}. As demonstrated in Fig. 4d, the almost complete quenching of PL intensity in Au@A-FH TiO_2/Ti suggests the highest efficiency of photogenerated e^-–h^+ separation.

Later, the charge separation (η_{sep}) and injection efficiency (η_{inj}) of all photoelectrodes are quantified using a hole scavenger of Na_2SO_3 based on the following equations:

$$\eta_{sep} = \frac{J_{Na_2SO_3}}{J_{abs}} \tag{2}$$

$$\eta_{inj} = \frac{J_{Na_2SO_4}}{J_{Na_2SO_3}} \tag{3}$$

where $J_{Na_2SO_3}$ is the photocurrent density in Na_2SO_3 oxidation (Fig. S6b, ESI†). The related statistics and findings are shown in Table S3 (ESI†) and Fig. 5. The J_{abs} is the theoretical maximum photocurrent density, which can be calculated from the UV-vis absorption spectrum and AM 1.5G solar spectrum with the following equation:

$$J_{abs} = \int_{300}^{\lambda_e} \frac{\lambda}{1240} \times \phi AM\ \ 1.5G(\lambda) \times LHE\ \ d\lambda \tag{4}$$

$$LHE = 1 - 10^{-A(\lambda)} \tag{5}$$

where λ_e is the absorption edge wavelength of the UV-vis absorption spectrum, φAM 1.5G(λ) in Fig. 5a is the reference

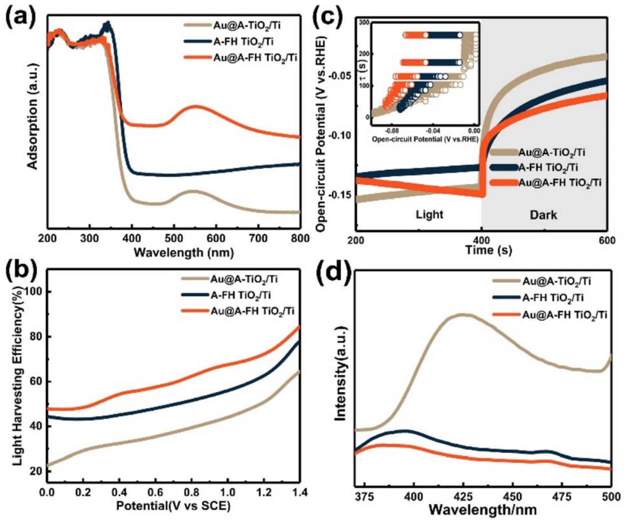

Fig. 4 (a) UV-vis-DRS spectra; (b) light absorption efficiency; (c) open-circuit voltage decay (V_{oc}) and average electron lifetimes (τ); (d) PL spectra of Au@A-TiO_2/Ti, A-FH TiO_2/Ti and Au@A-FH TiO_2/Ti.

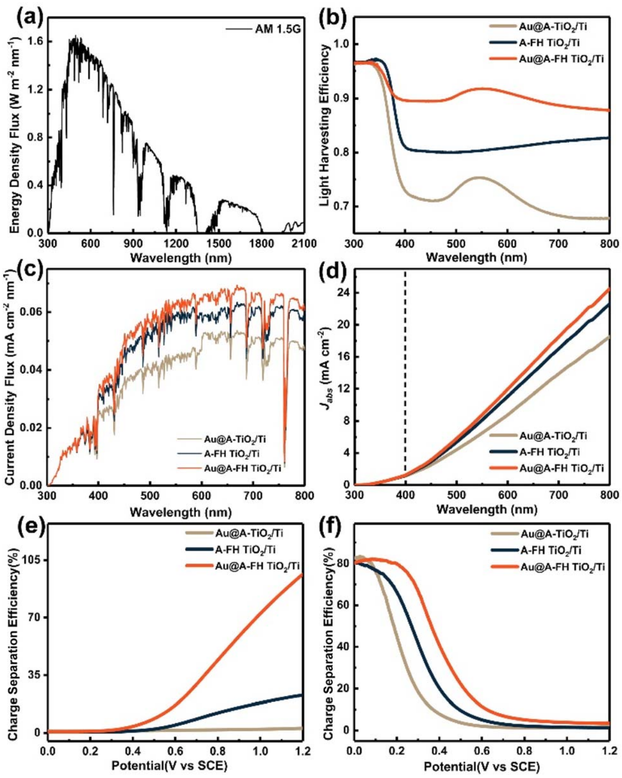

Fig. 5 (a) Energy density flux of the AM 1.5G standard solar spectrum. (b) Calculated light harvesting efficiency (LHE). (c and d) Current density flux and the theoretical maximum photocurrent intensity of three samples. (e) η_{sep} and (f) η_{inj} of Au@A-TiO_2/Ti, A-FH TiO_2/Ti and Au@A-FH TiO_2/Ti.

spectra derived from SMARTS v. 2.9.2 (W m^{-2} nm^{-1}), and $A(\lambda)$ is the absorbance at wavelength λ. Fig. 5b shows the theoretical light capture efficiency (LHE) from the UV-vis diffuse reflection image, in which Au@A-FH-TiO_2/Ti demonstrates the highest LHE. The J_{abs} can be obtained by integrating the current density fluxes of the three photoelectrodes between 300 and 800 nm (Fig. 5c). As illustrated in Fig. 4a, the absorption sidebands of all samples are 400 nm, and the highest J_{abs} at this wavelength is assigned to Au@A-FH-TiO_2/Ti as 1.125 mA cm^{-3} (Fig. 5d).

The values of η_{sep} at +0.4 V for Au@A-TiO_2/Ti, A-FH-TiO_2/Ti and Au@A-FH-TiO_2/Ti are 1.1%, 1.3% and 3.9%, respectively (Fig. 5e). The highest η_{sep} of Au@A-FH-TiO_2/Ti is presumably attributed to the synergistic effect of Au/TiO_2 Schottky junction and the {001}/{101} FH. Furthermore, Au@A-TiO_2/Ti has the highest η_{inj} of 40.8% at +0.4 V (Fig. 5f), which is much larger than those of Au@A-TiO_2/Ti (7.9%) and A-FH TiO_2/Ti (20.2%). This suggests the role of oxygen vacancies introduced during the photodeposition of Au NPs, which achieves the effective hole injection between the Au@A-FH-TiO_2/Ti and H_2O interface. Therefore, the above results demonstrate that the Au NPs and the introduction of FH allow for outstanding PEC catalysis performance.

3.4 *In situ* KPFM analyses and charge transfer mechanism

Charge transfer leads to a change in the surface work function in different regions, expressed as a variation in contact potential difference (CPD).[40] To further investigate the surface charge transfer process on the surface of of Au@A-FH TiO_2/Ti, the *in situ* KPFM was used to capture the CPD between the single Au NP and TiO_2 (Fig. 6a and b) in various environments. Fig. 6a and c separately show the AFM and the TEM-EDS mapping images between single Au NP and TiO_2, which agree with the SEM results. Fig. 6b1–b3 show the *in situ* KPFM potential figures in the dark, UV and visible light, respectively. The brighter color of the KPFM images indicates a higher electron concentration. It can be observed that the surface potential (V_{CPD}) decreases in all cases when the Au@A-FH TiO_2/Ti is illuminated. Electron–hole pairs are induced after the Au@A-FH TiO_2/Ti is irradiated with a certain wavelength of light, the holes are more inclined to reach the surface, thus reducing the surface electron concentration and leading to lower V_{CPD}. The specific cross-line V_{CPD} values along the dashed arrow (Fig. 6a) between the individual Au NP and TiO_2 are summarized in Fig. 6d. Under dark conditions, the V_{CPD} of Au NP is higher than that of the surrounding TiO_2, attributing to the higher theoretical work function of Au (5.1 eV) over TiO_2 (4.2 eV), which facilitates to form the metal–semiconductor Schottky junction and leads electron to transfer from TiO_2 to the surface Au NP. A similar result is obtained under UV illumination, and the V_{CPD} difference in Au/TiO_2 interface is more pronounced. This is mainly because TiO_2 absorbs the major part of UV light, producing more photogenerated e^- to accumulate on Au NP. Notably, in the case of visible light, a situation exactly opposite to the above condition is observed. The V_{CPD} of Au NP is lower than that of the TiO_2 nearby. At this time, the high-energy charges transfer from Au NP to TiO_2 through Au/TiO_2 Schottky junction.

By combining the Mott–Schottky curves and the UV-vis diffuse reflectance spectra (Fig. S7, ESI†), the conduction band (E_{CB}) and valence band (E_{VB}) positions of TiO_2 were calculated to be −0.75 V and 2.42 eV (*vs.* NHE),[41] respectively. According to the related literature and our previous studies, the energy band arrangement between {001} and {101} facets of TiO_2 presents a good step-like matching, which develops {001}/{101} FH.[25,42] Therefore, the charge transfer mechanism between Au and TiO_2 under visible light is proposed in Fig. 6e. At this time, only Au NP can be excited to generate plasmonic-induced electrons, which further cross the Au/TiO_2 Schottky junction and then injected into the TiO_2. For the Au NPs deposited on the highly exposed {001} facet, the energetic electrons from the Au LSPR effect fail to reflow owing to the Au–TiO_2 Schottky barrier and continue to move from {001} facet to {101} facet along the {001}/{101} FH. The {101} facet acts as a secondary separation intermediate station, which allows

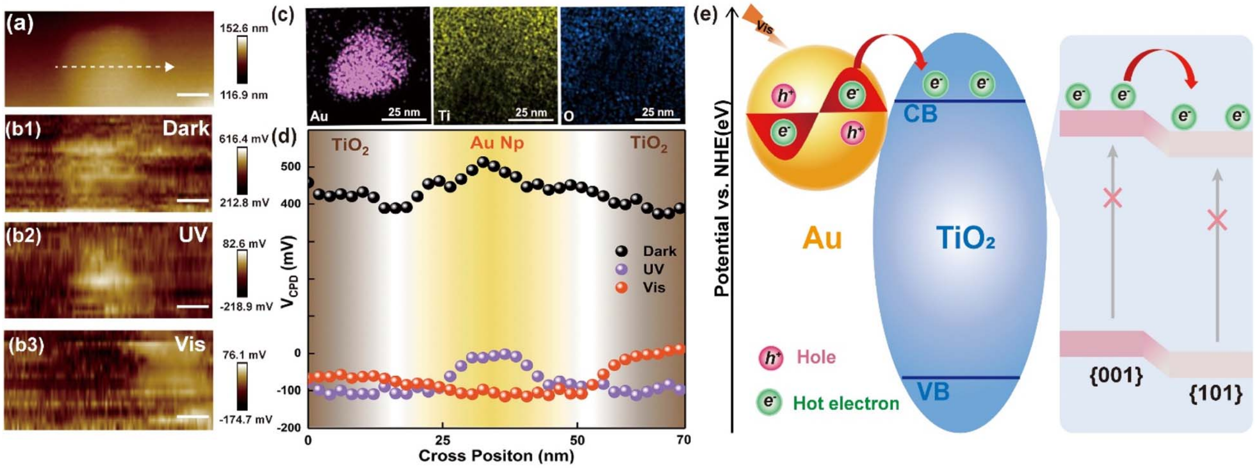

Fig. 6 (a) AFM and (c) TEM-EDS mapping images of Au@A-FH-TiO_2/Ti. V_{CPD} images between single Au NP and TiO_2 (b1) in the dark, (b2) UV and (b3) visible light. Scale bars, 10 nm. (d) V_{CPD} profiles of various environments. (e) The charge transfer mechanism between Au and TiO_2 under visible light.

electrons to finally arrive at the Ti network substrate. However, for the few Au NPs loaded onto the {101} facet, they are poorly excited to provide enough electrons because of the small exposure ratio and the mutual blockage of {101} facets. Through the synergy of Au/TiO_2 Schottky junction and {001}/{101} FH, the plasmonic-induced charges achieve efficient separation and become capable of facilitating efficient PEC reactions.

3.5 Removal of MO under the visible light

The PEC oxidation ability of Au@A-FH-TiO_2/Ti was verified by treating the typical dye contaminant methyl orange (MO) under visible light. As shown in Fig. 7a, the negligible degradation ability of A-FH TiO_2/Ti is owing to its wide band gap (3.17 eV), resulting in virtually non-absorption of visible light (Fig. S8, ESI†). As expected, the removal efficiency of Au@A-FH-TiO_2/Ti towards MO within 2 h is 94.3% (Fig. 7a) with a rate constant of 0.021 min^{-1} (the inset in Fig. 7a), which is 3.7 times as high as that obtained over A-FH TiO_2/Ti. Similarly, the total organic carbon (TOC) removal efficiency of Au@A-FH-TiO_2/Ti for MO reaches 90.89% within 6 h, showing remarkably thorough mineralization ability (Fig. 7d). Afterwards, the main active species in the degradation process under visible light are studied. N_2 and isopropanol (IPA) are used as the quenchers of $^{\bullet}O_2^-$ and $^{\bullet}OH$, respectively. Fig. 7b and e indicate that the quenching of $^{\bullet}O_2^-$ (indirectly produced by O_2 and e^-) significantly inhibits the degradation efficiency of MO from 93.9% to 60.6%, quenching off the $^{\bullet}OH$ directly from h^+ would slightly reduce the degradation efficiency by 11.5%, which affirms the dominant role of $^{\bullet}O_2^-$ in the degradation process. The corresponding equations are as follows:[42]

$$TiO_2 + h\nu \rightleftharpoons h^+ + e^- \tag{6}$$

$$h^+ + H_2O \rightleftharpoons {}^{\bullet}OH + H^+ \tag{7}$$

$$e^- + O_2 \rightleftharpoons O_2^{\bullet -} \tag{8}$$

The electron paramagnetic resonance (EPR) test was used to further verify the generation of $^{\bullet}O_2^-$ and $^{\bullet}OH$. As illustrated in Fig. 7c and f, the $^{\bullet}O_2^-$ and $^{\bullet}OH$ signal of Au@A-FH-TiO_2/Ti is significantly stronger than that of A-FH TiO_2/Ti. Moreover, the signal of $^{\bullet}O_2^-$ is stronger than that of $^{\bullet}OH$. The above results are speculated to be the reason for the high PEC performance.

Moreover, five reuse cycles of MO degradation are performed over Au@A-FH-TiO_2/Ti, and 91.6% removal of MO was still achieved with no significant changes on the photoelectrode surface (Fig. 8 and S9, ESI†). The XPS spectra in Fig. S10 (ESI†) show that the spectra of Ti 2p, O 1s and Au 4f before and after the PEC reaction are almost identical. These results collectively indicate the good stability and reusability of the prepared photoelectrode. Considering the presence of some colorless organic pollutants in the actual wastewater,[43] such as phenol and bisphenol A (BPA), the photoelectrode was also used to handle these pollutants. The results in Fig. S11† suggested that the Au@A-FH TiO_2/Ti removed 93.6% of phenol and 95.5% of BPA within 3 h, indicating promising application potential.

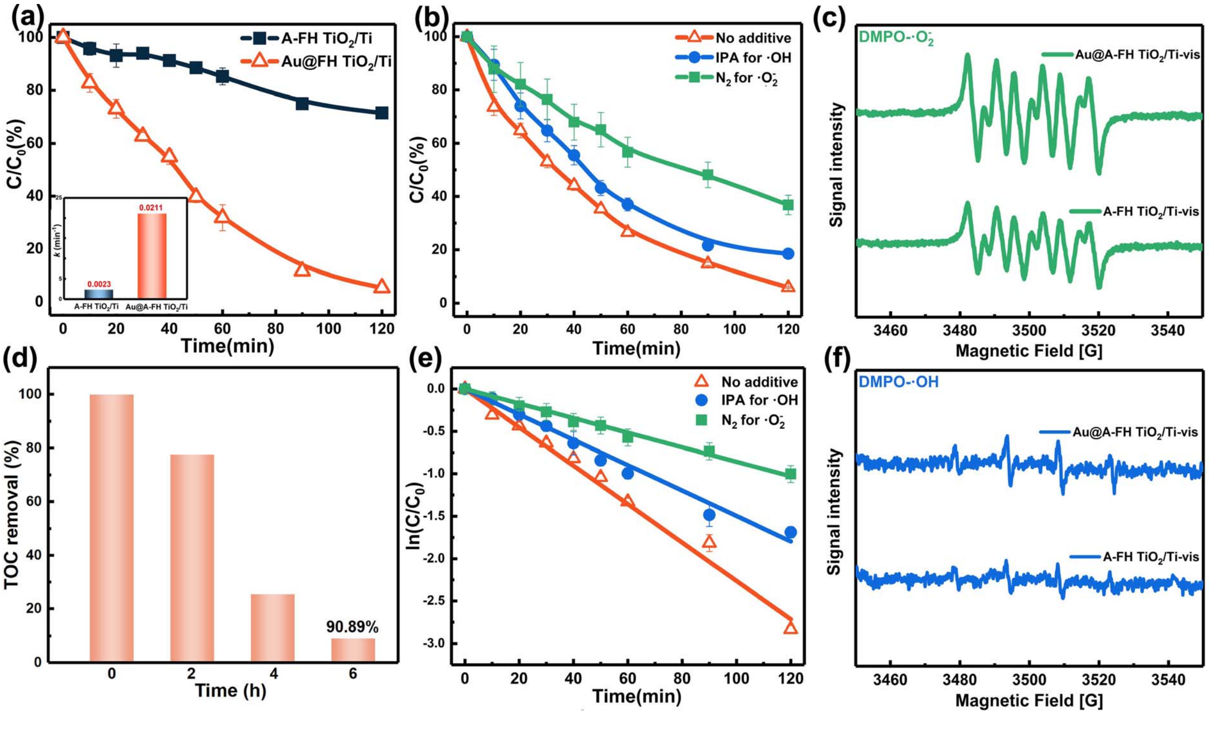

Fig. 7 (a) The degradation and first order kinetic curves with error bars for MO degradation on A-FH TiO_2/Ti and Au@A-FH-TiO_2/Ti, (b) TOC removal rate during MO degradation, (c and d) the scavenger quenching and first order kinetic curves for MO degradation, and (e and f) EPR spectra of A-FH TiO_2/Ti and Au@A-FH-TiO_2/Ti systems.

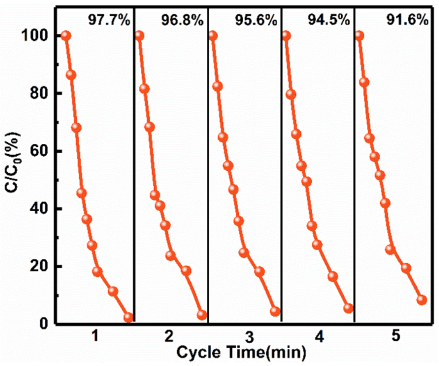

Fig. 8 Cycle experiments for PEC degradation of MO.

4. Conclusion

In conclusion, Au@A-FH-TiO_2/Ti photoelectrode was obtained by the photoreduction loading of Au NPs on the surface of flowerlike TiO_2 nano–microspheres with {001}/{101} FH. The charge transfer directions in the dark, UV and visible environments were clarified using *in situ* KPFM tests. Au@A-FH-TiO_2/Ti photoelectrode achieved almost 100% removal of MO under visible light in 2 h, and the degradation efficiency was still maintained at 91.6% after five cycles. The LSPR effect of Au NPs broadens the spectral absorption range. The Au/TiO_2 Schottky junction and energy-level staggered {001}/{101} FH synergistically facilitate the fast charge separation, thus yielding the highly efficient PEC performance of Au@A-FH-TiO_2/Ti. This work provides a reliable and intuitive experimental methodology to verify the charge transfer mechanism, and also provides a novel channel for designing efficient TiO_2-based visible light responsive photoelectrodes for the efficient removal of organic dyes and other non-dye pollutants.

Author contributions

Pan Zhang: writing-original draft, conceptualization, investigation, formal analysis; Yuzhou Jin: investigation, formal analysis; Mingfang Li: technical assistance, writing-review; Xuejiang Wang: investigation, technical assistance, Ya-nan Zhang: investigation, funding acquisition, writing-review.

Conflicts of interest

There are no conflicts to declare.

Acknowledgements

This work was supported by National Natural Science Foundation of China (NSFC, No. 22276136, 21876133), Natural Science Foundation of Shanghai (No. 20ZR1462500), the Science & Technology Commission of Shanghai Municipality (No. 14DZ2261100) and the Fundamental Research Funds for the Central Universities (No. 22120210531, 2022-4-YB-1B).

Notes and references

1 J. Zhang, G. Zhang, H. Lan, J. Qu and H. Liu, *Environ. Sci. Technol.*, 2021, **55**, 3296–3304.

2 M. G. Lee, J. W. Yang, H. Park, C. W. Moon, D. M. Andoshe, J. Park, C. K. Moon, T. H. Lee, K. S. Choi, W. S. Cheon, J. J. Kim and H. W. Jang, *Nano-Micro Lett.*, 2022, **14**, 48.

3 Y. Yang, J. J. Pignatello, J. Ma and W. A. Mitch, *Environ. Sci. Technol.*, 2014, **48**, 2344–2351.

4 D. Yuan, M. Sun, S. Tang, Y. Zhang, Z. Wang, J. Qi, Y. Rao and Q. Zhang, *Chin. Chem. Lett.*, 2020, **31**, 547–550.

5 A. K. Biń and S. Sobera-Madej, *Ozone: Sci. Eng.*, 2012, **34**, 136–139.

6 C. A. Martínez-Huitle and M. Panizza, *Curr. Opin. Electrochem.*, 2018, **11**, 62–71.

7 Q. Ma, R. Song, F. Ren, H. Wang, W. Gao, Z. Li and C. Li, *Appl. Catal., B*, 2022, **309**, 121292.

8 L. Liu, P. Li, T. Wang, H. Hu, H. Jiang, H. Liu and J. Ye, *Chem. Commun.*, 2015, **51**, 2173–2176.

9 T. Zhou, S. Chen, L. Li, J. Wang, Y. Zhang, J. Li, J. Bai, L. Xia, Q. Xu, M. Rahim and B. Zhou, *Appl. Catal., B*, 2020, **269**, 118776.

10 F. Wu, Y. Yu, H. Yang, L. N. German, Z. Li, J. Chen, W. Yang, L. Huang, W. Shi, L. Wang and X. Wang, *Adv. Mater.*, 2017, **29**, 1701432.

11 R. Song, H. Chi, Q. Ma, D. Li, X. Wang, W. Gao, H. Wang, X. Wang, Z. Li and C. Li, *J. Am. Chem. Soc.*, 2021, **143**, 13664–13674.

12 Q. Niu, X. Gu, L. Li, Y.-n. Zhang and G. Zhao, *Appl. Catal., B*, 2020, **261**, 118229.

13 P. Zhang, X. Gu, N. Qin, Y. Hu, X. Wang and Y. N. Zhang, *J. Hazard. Mater.*, 2023, **441**, 129896.

14 X. Zheng, H. Guo, Y. Xu, J. Zhang and L. Wang, *J. Mater. Chem. C*, 2020, **8**, 13836–13842.

15 M. Y. Ye, Z. H. Zhao, Z. F. Hu, L. Q. Liu, H. M. Ji, Z. R. Shen and T. Y. Ma, *Angew. Chem., Int. Ed. Engl.*, 2017, **56**, 8407–8411.

16 H. Li and L. Zhang, *Nanoscale*, 2014, **6**, 7805–7810.

17 C. Boerigter, R. Campana, M. Morabito and S. Linic, *Nat. Commun.*, 2016, **7**, 10545.

18 S. T. Kochuveedu, Y. H. Jang and D. H. Kim, *Chem. Soc. Rev.*, 2013, **42**, 8467–8493.

19 Z. Bian, T. Tachikawa, P. Zhang, M. Fujitsuka and T. Majima, *J. Am. Chem. Soc.*, 2014, **136**, 458–465.

20 A. Kumar, M. Khan, J. He and I. M. C. Lo, *Water Res.*, 2020, **170**, 115356.

21 H. Zhao, X. Liu, Y. Dong, Y. Xia, H. Wang and X. Zhu, *ACS Appl. Mater. Interfaces*, 2020, **12**, 31532–31541.

22 D. Gogoi, A. K. Shah, P. Rambabu, M. Qureshi, A. K. Golder and N. R. Peela, *ACS Appl. Mater. Interfaces*, 2021, **13**, 45475–45487.

23 Y. Hu, Y. Jin, P. Zhang, Y.-n. Zhang and G. Zhao, *Appl. Catal., B*, 2023, **322**, 122102.

24 J. Yu, J. Low, W. Xiao, P. Zhou and M. Jaroniec, *J. Am. Chem. Soc.*, 2014, **136**, 8839–8842.

25 S. Han, Q. Niu, N. Qin, X. Gu, Y. N. Zhang and G. Zhao, *Chem. Commun.*, 2020, **56**, 1337–1340.

26 X. Gu, N. Qin, G. Wei, Y. Hu, Y. N. Zhang and G. Zhao, *Chemosphere*, 2021, **263**, 128257.

27 C. P. Sajan, S. Wageh, A. A. Al-Ghamdi, J. Yu and S. Cao, *Nano Res.*, 2015, **9**, 3–27.

28 J. Yu, G. Dai, Q. Xiang and M. Jaroniec, *J. Mater. Chem.*, 2011, **21**, 1049–1057.

29 X. Liu, G. Dong, S. Li, G. Lu and Y. Bi, *J. Am. Chem. Soc.*, 2016, **138**, 2917–2920.

30 H. Zhang, X. Liu, Y. Wang, P. Liu, W. Cai, G. Zhu, H. Yang and H. Zhao, *J. Mater. Chem. A*, 2013, **1**, 2646–2652.

31 M.-Y. Xing, B.-X. Yang, H. Yu, B.-Z. Tian, S. Bagwasi, J.-L. Zhang and X.-Q. Gong, *J. Phys. Chem. Lett.*, 2013, **4**, 3910–3917.

32 J. Yu, G. Dai, Q. Xiang and M. Jaroniec, *J. Mater. Chem.*, 2011, **21**, 1049–1057.

33 Y. Lu, X. Liu, H. Liu, Y. Wang, P. Liu, X. Zhu, Y. Zhang, H. Zhang, G. Wang, Y. Lin, H. Diao and H. Zhao, *Small Struct.*, 2020, **1**, 202000025.

34 L. K. Preethi, T. Mathews, M. Nand, S. N. Jha, C. S. Gopinath and S. Dash, *Appl. Catal., B*, 2017, **218**, 9–19.

35 J. Qi, X. Yang, P. Y. Pan, T. Huang, X. Yang, C. C. Wang and W. Liu, *Environ. Sci. Technol.*, 2022, **56**, 5200–5212.

36 R. Siavash Moakhar, G. K. L. Goh, A. Dolati and M. Ghorbani, *Appl. Catal., B*, 2017, **201**, 411–418.

37 D. Ding, K. Liu, S. He, C. Gao and Y. Yin, *Nano Lett.*, 2014, **14**, 6731–6736.

38 G. Yang, Y. Li, H. Pang, K. Chang and J. Ye, *Adv. Funct. Mater.*, 2019, **29**, 1904622.

39 H. Li, S. Wang, M. Wang, Y. Gao, J. Tang, S. Zhao, H. Chi, P. Zhang, J. Qu, F. Fan and C. Li, *Angew. Chem., Int. Ed. Engl.*, 2022, **61**, e202204272.

40 R. Chen, Z. Ren, Y. Liang, G. Zhang, T. Dittrich, R. Liu, Y. Liu, Y. Zhao, S. Pang, H. An, C. Ni, P. Zhou, K. Han, F. Fan and C. Li, *Nature*, 2022, **610**, 296–301.

41 T. Zhou, S. Chen, L. Li, J. Wang, Y. Zhang, J. Li, J. Bai, L. Xia, Q. Xu, M. Rahim and B. Zhou, *Appl. Catal., B*, 2020, **269**, 118776.

42 L. Hu, C. C. Fong, X. Zhang, L. L. Chan, P. K. Lam, P. K. Chu, K. Y. Wong and M. Yang, *Environ. Sci. Technol.*, 2016, **50**, 4430–4438.

43 S. Garcia-Segura and E. Brillas, *J. Photochem. Photobiol., C*, 2017, **31**, 1–35.